Spectrally Consistent Upscaling of Wind Speed Time Series Data

Marius Bittner[1,*], Parth Tambat[1], Marco Behrendt[2], and Michael Beer[1,3,4]
[1]*Institute for Risk and Reliability, Leibniz University Hannover, 30167 Hannover, Germany*
[*]*Corresponding author: bittner@irz.uni-hannover.de*
[2]*Department of Civil and Environmental Engineering, Rice University, Houston, USA*
[3]*Institute for Risk and Uncertainty, University of Liverpool, Liverpool, UK*
[4]*International Joint Research Center for Engineering Reliability and Stochastic Mechanics, Tongji University, Shanghai, China*

Abstract. As the share of wind energy grows, reliable engineering computations for wind speed modeling become critical for forecasting, stability assessment, and risk-informed design. A central challenge is that available wind records are often limited to coarse time averages, such as 10-minute or hourly means, which suffice for energy yield estimates but miss the high-frequency variability needed for reliability analysis, fatigue assessment, and extreme-event studies.

Building on the Temporal Enhanced Fourier Transform (TEFT), we develop an integrated storm-hazard reliability framework that transforms coarse storm wind histories into high-resolution structural loading scenarios. The approach estimates the spectrum implied by averaged data, corrects for attenuation due to temporal averaging, and reconstructs a finer time grid by adjusting Fourier coefficients under consistency constraints. These constraints enforce agreement with observed moments and marginal distributions, while stochastic sampling generates ensembles that reflect uncertainty. The procedure avoids direct reliance on measured high-rate data, yet maintains realistic maxima, means, variance, distributional fit, and spectral slope.

Results show that the generated high-resolution series align with observed characteristics and support reliability computations. The method enables more faithful storm-to-structure simulations for grid stability, structural reliability of onshore and offshore assets, and extreme-event risk analysis, thereby strengthening the reliability and reproducibility of engineering decisions for critical infrastructure systems.

Keywords: wind speed modeling, risk assessment in wind energy, stochastic wind simulation, high-resolution wind data, environmental processes

1. Introduction

High-frequency wind fluctuations can dominate short-duration structural demand, fatigue accumulation, and threshold exceedances, but many environmental wind archives are distributed only as time-averaged records. TEFT was introduced to reconstruct high-resolution wind-speed histories from coarse measurements while preserving statistical and spectral properties (Tambat et al., 2026). The resulting scale gap is especially relevant for tropical-cyclone and severe-storm scenarios, where a slowly varying storm envelope can coexist with reliability-relevant turbulent fluctuations.

Hybrid parametric and background-wind models have already been used to connect typhoon wind fields with port disruption and regional economic losses (Zhang et al., 2020; Tian et al., 2023). Artificial storm-track generation has likewise been used to construct targeted rare-event scenarios for coastal risk studies (Sun et al., 2022). The present work redirects these ideas toward structural reliability by coupling the storm wind-field layer with TEFT-based temporal refinement and OpenSees dynamic response analysis (McKenna et al., 2010).

The paper is organized around a modular hazard-to-response workflow. The methodology is summarized in Section 2, followed by a controlled fixed-storm TEFT benchmark and a stochastic storm-to-structure reliability example.

2. Methodology

The proposed framework couples tropical-cyclone wind-field simulation, spectrally consistent temporal upscaling, structural load generation, and dynamic reliability analysis. The workflow starts from best-track-like storm information, computes a coarse wind-speed history at the structure location, reconstructs a high-resolution wind signal using TEFT (Tambat et al., 2026), and propagates the resulting wind loads through a unit-consistent finite-element model. This structure keeps the hazard model, temporal refinement, and structural response model modular, so that deterministic storm scenarios and stochastic storm ensembles can be treated within the same computational pipeline at the desired level of modeling detail.

2.1. Storm Representation and Wind-Field Model

Each storm event is represented by a best-track-like table

$$\mathcal{B} = \{t_i, \phi_i, \lambda_i, p_{c,i}, V_{\max,i}, R_{\max,i}, u_{b,i}, v_{b,i}\}_{i=1}^{N}, \tag{1}$$

where t_i is time, ϕ_i and λ_i are the cyclone-center latitude and longitude, $p_{c,i}$ is central pressure, $V_{\max,i}$ is maximum wind speed, $R_{\max,i}$ is the radius of maximum wind speed, and $(u_{b,i}, v_{b,i})$ denotes the eastward and northward components of the background wind vector at the site. For deterministic examples, this table is prescribed. For stochastic examples, the table is generated from a small set of physically interpretable random variables. The current Monte Carlo results use random track geometry, central pressure, maximum intensity, background wind, and TEFT realization seed. $R_{\max}$ is not sampled independently in these Monte Carlo runs; it is computed inside the parametric wind model from central pressure, latitude, and translation speed. A separate stochastic one-shot prototype additionally samples $R_{\max}$ explicitly, but that variant is not the source of the reliability numbers reported in Section 3. This extends targeted artificial-track ideas used for synthetic superstorm studies (Sun et al., 2022) by randomizing a richer set of best-track and wind-field variables.

The stochastic modelling of tropical cyclones uses a quadratic-Bezier track generator in a local east–north coordinate system centered at the structure site. Let $\mathbf{e}(\alpha) = (\cos\alpha, \sin\alpha)^\top$ be the along-track unit vector for heading α, and $\mathbf{n}(\alpha) = (-\sin\alpha, \cos\alpha)^\top$ its left-normal direction. For each sample, the heading H, along-track extent L, closest-approach control distance D_c, curvature control κ, minimum pressure $p_{\min}$, maximum intensity cap $V_{\max}^{\mathrm{cap}}$, background-wind speed U_b, and background-wind direction Θ_b are drawn independently from bounded uniform distributions:

$$\begin{array}{ll} H \sim \mathrm{Unif}(150^\circ, 205^\circ), & L \sim \mathrm{Unif}(1900, 3000) \text{ km}, \\ D_c \sim \mathrm{Unif}(35, 140) \text{ km}, & \kappa \sim \mathrm{Unif}(0, 520) \text{ km}, \\ p_{\min} \sim \mathrm{Unif}(910, 945) \text{ hPa}, & V_{\max}^{\mathrm{cap}} \sim \mathrm{Unif}(54, 68) \text{ m/s}, \\ U_b \sim \mathrm{Unif}(2, 10) \text{ m/s}, & \Theta_b \sim \mathrm{Unif}(-120^\circ, 40^\circ). \end{array} \tag{2}$$

All angles are measured counterclockwise from east. A common ocean-side genesis region is imposed through the reference heading $H_{\mathrm{ref}} = 160^\circ$ and start distance $D_0 = 1050$ km:

$$\mathbf{P}_0 = -D_0 \mathbf{e}(H_{\mathrm{ref}}), \qquad \mathbf{P}_2 = \mathbf{P}_0 + L\mathbf{e}(H). \tag{3}$$

The quadratic Bezier control point is then chosen as

$$\mathbf{P}_1 = 2D_c \mathbf{n}(H) - \frac{1}{2}(\mathbf{P}_0 + \mathbf{P}_2) + \kappa \mathbf{n}(H), \tag{4}$$

and the storm centerline is

$$\mathbf{P}(\tau) = (1-\tau)^2 \mathbf{P}_0 + 2(1-\tau)\tau \mathbf{P}_1 + \tau^2 \mathbf{P}_2, \qquad 0 \le \tau \le 1. \tag{5}$$

The $N = 21$ best-track rows are evaluated at $\tau_i = (i-1)/(N-1)$, using 6 h spacing. The local coordinates $\mathbf{P}(\tau_i)$ are converted to latitude and longitude by a local geodetic offset. The parameter D_c should be interpreted as a closest-approach control rather than an exact realized minimum distance: the curvature term shifts the mid-track point to $(D_c + \kappa/2)\mathbf{n}(H)$, and the actual minimum site distance follows from the full sampled curve.

The pressure and intensity histories are smooth functions of the normalized track coordinate $u = 2\tau - 1$:

$$p_c(\tau) = p_{\mathrm{outer}} - (p_{\mathrm{outer}} - p_{\min}) \exp(-3u^2), \tag{6}$$

with $p_{\mathrm{outer}} = 1000$ hPa in the reported runs. The maximum wind speed parameter is linked to the pressure deficit by

$$V_{\max}(\tau) = V_{\min} + \eta(\tau)^{0.65} \left(V_{\max}^{\mathrm{cap}} - V_{\min}\right), \qquad \eta(\tau) = \frac{p_{\mathrm{env}} - p_c(\tau)}{p_{\mathrm{env}} - p_{\min}}, \tag{7}$$

where $V_{\min} = 18$ m/s and $p_{\mathrm{env}} = 1010$ hPa. The background wind is constant within one sample, $(u_b, v_b) = U_b(\cos\Theta_b, \sin\Theta_b)$, but varies between samples.

At each time step, the wind vector at a site is obtained from a hybrid parametric cyclone model. Following the broad structure used in typhoon-induced port-disruption studies (Zhang et al., 2020; Tian et al., 2023), the storm-relative wind is decomposed into a moving component and a rotating component, and then blended with the background wind:

$$\mathbf{v}(t) = (1 - e(r))\, \mathbf{v}_{tc}(t) + e(r)\mathbf{v}_b(t), \tag{8}$$

with

$$e(r) = \frac{c^4}{1 + c^4}, \qquad c = \frac{r}{nR_{\max}}. \tag{9}$$

Here r is the distance from the cyclone center to the site and n controls the transition from cyclone-dominated to background-dominated flow. The vector $\mathbf{v}_{tc}(t)$ is the sum of the storm translation and rotating cyclone components, $\mathbf{v}_b(t) = (u_b(t), v_b(t))^\top$ is the background wind, c is the radius normalized by $nR_{\max}$, and $e(r)$ is the corresponding hybrid blending weight. In the current Monte Carlo runs, the radius of maximum wind is derived as

$$R_{\max} = \left[a_R \tanh\{b_R(\phi - 28)\} + c_R \exp\left(\frac{p_{\mathrm{env}} - p_c}{33.86}\right) + d_R V_{\mathrm{tr}} + e_R\right] 1000, \tag{10}$$

where ϕ is storm-center latitude, V_{tr} is translation speed. The coefficients are

$$(a_R, b_R, c_R, d_R, e_R) = (28.52, 0.0873, 12.22, 0.2, 37.22). \tag{11}$$

The bracketed value is in kilometres and is converted to metres before evaluating the wind field. The resulting coarse wind-speed history is the Euclidean norm

$$U_c(t_k) = \|\mathbf{v}(t_k)\|_2\,, \tag{12}$$

evaluated on a regular time grid, here using 10-minute spacing.

2.2. Threshold-Triggered TEFT Upscaling

The high-frequency wind content is reconstructed only during dynamically relevant storm periods. A TEFT window is triggered when the coarse site wind speed exceeds a prescribed threshold U_{thr}. Padding is added before and after the triggered interval so that the upscaling captures the surrounding storm envelope.

Let $U_c(t_k)$ denote the coarse wind-speed samples with time step ΔT. The coarse signal is separated into a slowly varying trend and a fluctuating component,

$$U_c(t_k) = m_c(t_k) + u'_c(t_k). \tag{13}$$

The Fourier amplitudes of u'_c are estimated from the coarse record. Because coarse samples represent time-averaged wind speeds, the resolved spectrum is corrected for attenuation by the temporal averaging operation. The unresolved high-frequency Fourier coefficients are then extrapolated according to the estimated spectral decay, while the total variance is constrained to match a target turbulence level.

A fine-grid fluctuation $u'_f(t)$ is synthesized by combining the corrected and extrapolated Fourier amplitudes with stochastic phases. An iterative amplitude adjusted Fourier transform step is used to preserve the target marginal distribution and moment constraints. The final high-resolution wind history is constructed as

$$U_f(t) = m_f(t) + a(t)u'_f(t), \tag{14}$$

where $m_f(t)$ is the interpolated storm-scale trend and $a(t)$ is a time-varying turbulence envelope derived from the coarse storm history. In the implementation, a preliminary envelope is computed from the interpolated trend relative to the coarse-window mean,

$$\tilde{a}(t) = \max\left(\frac{m_f(t)}{\overline{U}_c}, a_{\min}\right), \tag{15}$$

where $a_{\min}$ is an envelope floor. The envelope is then RMS-normalized,

$$a(t) = \frac{\tilde{a}(t)}{\left(\frac{1}{|\mathcal{T}|}\int_{\mathcal{T}} \tilde{a}^2(\tau)\, d\tau\right)^{1/2}}, \tag{16}$$

so that it redistributes the target turbulent standard deviation over time without changing its window-scale energy. This gives a separable evolutionary spectral representation,

$$S(t, f) = a^2(t) S_{\mathrm{TEFT}}(f), \tag{17}$$

where $S_{\mathrm{TEFT}}(f)$ is the one-sided spectrum implied by the corrected and extrapolated TEFT Fourier amplitudes of the stationary fluctuation $u'_f(t)$. This preserves the non-stationary cyclone envelope while restoring high-frequency variability relevant for structural response.

2.3. Wind Load Generation and Structural Response

The refined wind-speed history is converted to nodal wind loads for the finite-element model. For each loaded structural node j, the wind load is computed from the local wind speed using a Eurocode-style aerodynamic load model (European Committee for Standardization, 2005), including height-dependent exposure and force coefficients:

$$F_j(t) = \frac{1}{2}\rho C_j A_j U_j^2(t). \tag{18}$$

The resulting load histories are written as OpenSees input files and applied to the structural model as time-dependent nodal loads.

The structural model used in the numerical examples is a 50 m steel lattice tower idealized as a cantilever truss-type structure in OpenSees (McKenna et al., 2010). The tower is discretized by 17 nodes and 16 beam-column elements, as shown schematically in panel (a) of Figure 1. Nodes 1–16 correspond to the wind-loaded tower sections, while Node 17 is fixed at the base. Section-dependent aerodynamic areas, enclosed areas, reference heights, and lumped masses are assigned according to the tower documentation. The lumped mass distribution follows the enclosed-area allocation

$$m_i = M_{\mathrm{tot}} \frac{A_i^{\mathrm{enc}}}{\sum_k A_k^{\mathrm{enc}}}, \qquad M_{\mathrm{tot}} = 13\,172 \text{ kg}. \tag{19}$$

The section stiffnesses are derived from the lattice-support approximation

$$I_{\mathrm{eff}} = 0.5 h_0^2 A_{\mathrm{ch}}, \tag{20}$$

where h_0 is the section width and A_{ch} is the total cross-sectional area of the main chord members. In the present numerical examples the nominal Young's modulus is $E = 2.1 \cdot 10^8$ kN/m^2.

The structural response is evaluated by solving the dynamic equilibrium equation

$$\mathbf{M}\ddot{\mathbf{q}}(t) + \mathbf{C}\dot{\mathbf{q}}(t) + \mathbf{K}\mathbf{q}(t) = \mathbf{F}(t), \tag{21}$$

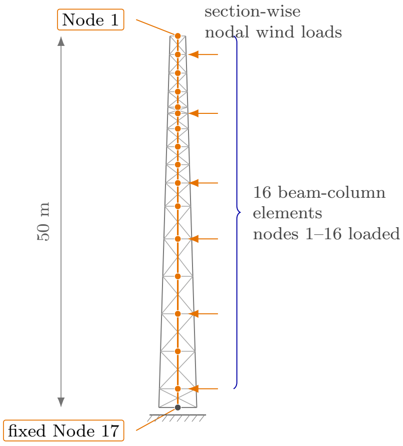

(a) Truss tower idealization.

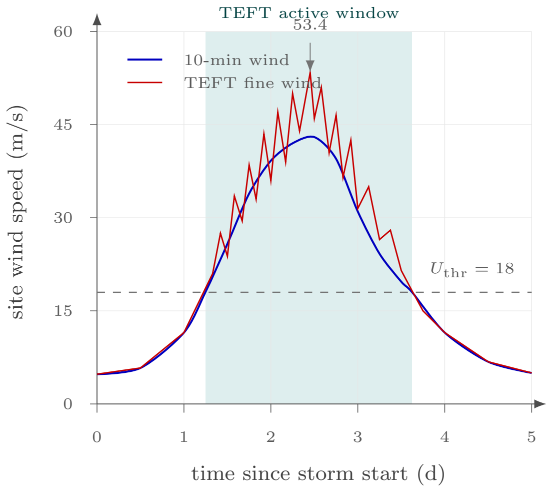

(b) Threshold-triggered storm wind history.

Figure 1. Coupled structural and wind-loading representation used in the numerical examples. The tower idealization defines the nodal load application points, while the site wind-speed history illustrates the threshold-triggered TEFT refinement that supplies high-resolution dynamic loading during the storm core.

where $\mathbf{q}(t)$ contains the structural degrees of freedom and $\mathbf{F}(t)$ is the vector of wind-induced nodal loads. The present numerical examples extract response histories and peak nodal displacements after each OpenSees simulation. To avoid evaluating the initial transient caused by sudden load application, peak displacement metrics are computed only after the first 20 s of simulated response.

2.4. Reliability Formulation

For stochastic analyses, the random input vector X may include storm-track parameters, pressure deficit, maximum wind speed, $R_{\max}$, background wind, TEFT phase realization, turbulence intensity, and structural parameters. The performance function is defined in terms of the maximum absolute top-node displacement:

$$g(X) = d_{\text{cap}} - \max_t |d_{\text{top}}(t; X)|. \tag{22}$$

Failure occurs when $g(X) \leq 0$, and the failure probability is estimated by Monte Carlo simulation as

$$\hat{P}_f = \frac{1}{N_s} \sum_{s=1}^{N_s} \mathbf{1}\left[g(X_s) \leq 0\right]. \tag{23}$$

This formulation allows the same framework to support deterministic one-shot demonstrations, stochastic best-track scenarios, and full storm-to-structure reliability simulations.

2.5. Computational Implementation

The computational workflow is implemented as a Julia package `StormHazards` (Bittner, 2026; Bezanson et al., 2017). It couples parametric storm simulation, TEFT upscaling, load generation, and reliability orchestration, and uses OpenSees for dynamic structural response (McKenna et al., 2010). Monte Carlo sampling and external-model execution are managed through UncertaintyQuantification.jl (Behrensdorf et al., 2023; Behrensdorf et al., 2026), with SLURM scripts used for cluster-scale runs. Each module exchanges explicit tabular data products, including best-track tables, wind histories, load histories, response histories, and figure-ready CSV files. This makes the framework practical and modular: the storm generator, temporal-upscaling method, structural solver, or reliability estimator can be replaced without changing the complete pipeline.

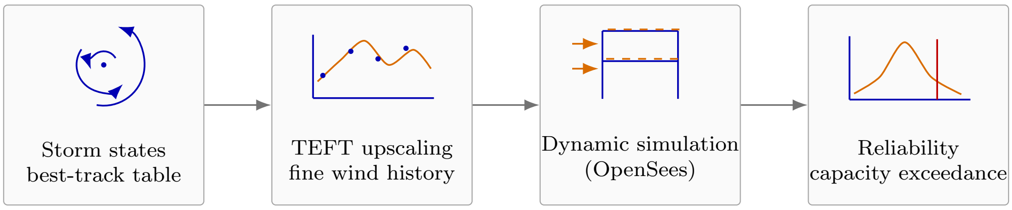

Figure 2. Modular storm-to-reliability workflow. The implementation keeps the storm description, temporal reconstruction, structural analysis, and reliability calculation as separate exchangeable stages connected by auditable data files.

3. Numerical Results

Two $N = 1000$ truss-tower simulations are used to separate the effect of temporal wind upscaling from the effect of storm-to-storm variability. The first run, denoted here as the controlled TEFT benchmark, keeps the single synthetic storm history, background wind, structural model, and capacity fixed, and samples only the unresolved TEFT-EPSD wind realization. The second run samples the artificial best-track geometry, intensity parameters, background-wind vector, and TEFT realization before propagating each event through the same OpenSees tower model. Both runs use a demonstration site near Kowloon Bay, Hong Kong, $(22.3°\text{N}, 114.2°\text{E})$, a 10-minute coarse wind record, a 10 s refined time step, an 18 m/s trigger threshold, and the illustrative top-displacement capacity $d_{\text{cap}} = 0.25$ m.

Table I summarizes the two experiments. In the controlled benchmark, the maximum coarse site wind speed is 43.47 m/s. After TEFT-EPSD refinement, the sample-wise maximum wind speed has mean 52.14 m/s and reaches 66.95 m/s. The mean maximum absolute top-node displacement is 0.182 m, with 95th and 99th percentiles of 0.264 m and 0.288 m, respectively. At the selected capacity, 93 of 1000 samples fail, giving $\hat{P}_f = 0.093$ with Monte Carlo standard error 0.0092. This run is therefore best interpreted as a controlled check of the TEFT-to-structure coupling: the storm envelope is fixed, but the unresolved temporal variability alone is sufficient to move part of the response distribution into the failure domain.

The stochastic storm ensemble adds storm-to-storm variability to the same OpenSees structural calculation. The random-variable definitions and ranges are given in Section 2.1, and Figure 3

Table I. Summary of the two 1000-sample truss-tower reliability runs. Wind maxima refer to sample-wise TEFT-refined maxima; displacement statistics refer to the maximum absolute top-node displacement.

Run	Main random variables	$\overline{U}_{\max}$ (m/s)	$U_{\max}$ (m/s)	d_{95} (m)	d_{99} (m)	$d_{\max}$ (m)	$\hat{P}_f$
Controlled TEFT benchmark	TEFT-EPSD realization	52.14	66.95	0.264	0.288	0.292	0.093
Stochastic storm ensemble	Track, intensity, background wind, TEFT-EPSD realization	47.82	77.87	0.274	0.321	0.395	0.093

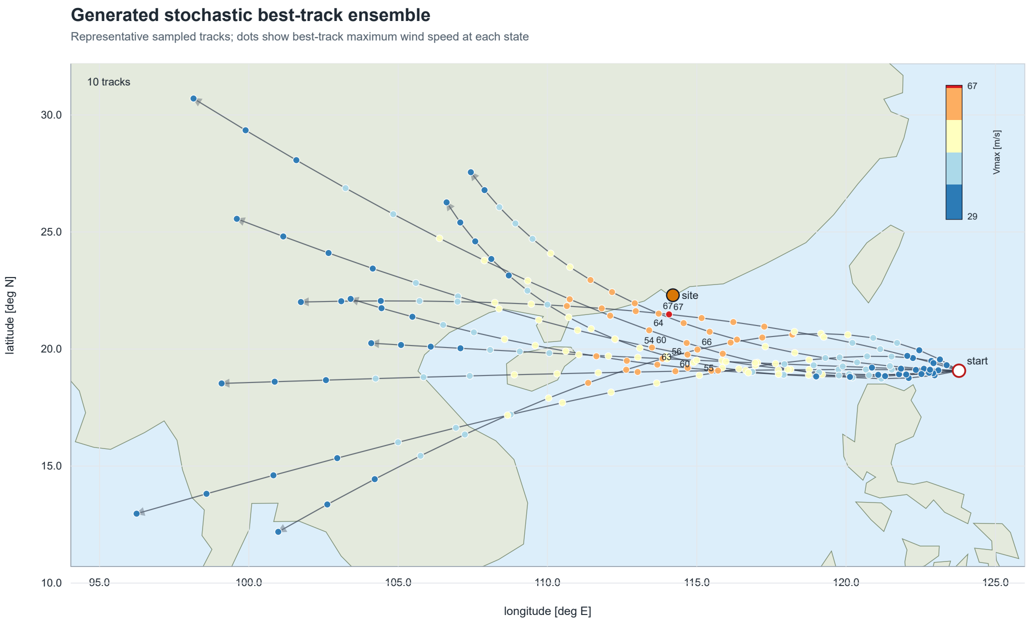

Figure 3. Generated stochastic best-track ensemble used as hazard input for the storm-to-structure simulations. The curves show representative sampled quadratic-Bezier storm tracks, while the colored best-track states indicate the evolving maximum wind-speed parameter along each artificial event. The figure documents the stochastic storm geometry before temporal upscaling and structural propagation.

visualizes representative sampled quadratic-Bezier best tracks before temporal upscaling and structural propagation. In the present 1000-sample run, the sampled coarse-wind ensemble has mean maximum speed 42.90 m/s and reaches 54.29 m/s; after TEFT-EPSD refinement the corresponding sample-wise wind maxima have mean 47.82 m/s and reach 77.87 m/s.

Figure 4 summarizes the wind input and the resulting top-node demand for the stochastic storm ensemble. The reliability calculation itself is evaluated from the maximum absolute top-node displacement defined in Eq. (22). In the wind diagnostic, the deterministic fixed-storm preview remains visible as a reference, while the sampled coarse-wind mean and the TEFT-refined ensemble describe the stochastic run.

The stochastic run produces a mean maximum absolute top-node displacement of 0.157 m and a median of 0.147 m, both below the corresponding controlled-run values of 0.182 m and 0.184 m. This decrease in central demand is expected because many sampled storms pass less unfavorably than the fixed benchmark track. The main difference appears in the upper tail: the 95th percentile increases from 0.264 m to 0.274 m, the 99th percentile increases from 0.288 m to 0.321 m, and the maximum observed top-node displacement increases from 0.292 m to 0.395 m. At $d_{\mathrm{cap}} = 0.25$ m, 93 of 1000 stochastic storm samples fail, giving $\hat{P}_f = 0.093$ with Monte Carlo standard error 0.0092. Thus, at the selected illustrative capacity, the two experiments give the same exceedance estimate, with both values obtained directly from the exported sample tables. They reach this estimate through different demand distributions: the stochastic storm ensemble has a lower center and a heavier extreme tail.

The height-wise displacement profile in Figure 5 shows that the largest responses occur at the upper tower nodes and decrease toward the base, as expected for the cantilever-type idealization. Across both runs, the top response node is also the critical node for the reported capacity exceedance. In the controlled benchmark the estimated exceedance probability drops to zero once the capacity exceeds 0.295 m. In the stochastic storm run, a nonzero exceedance tail remains up to the largest inspected capacity of 0.35 m, where 3 of 1000 samples still exceed the limit. This comparison is the clearest reliability effect of the second example: even when the probability at 0.25 m is unchanged, storm-parameter uncertainty controls the high-capacity tail.

The Fourier-coefficient and PSD diagnostics generated with the runs are retained as traceability outputs, but they are not all reproduced here. Their role is to verify the same TEFT steps described by Tambat et al. (Tambat et al., 2026): the resolved low-frequency body is inferred from the coarse record, the high-frequency tail is extrapolated, and the spectrum is rescaled to match the target turbulent standard deviation. The present framework differs by applying that reconstruction only inside the storm-triggered active window and by embedding it in the separable TEFT-EPSD representation $S(t, f) = a^2(t)S_{\mathrm{TEFT}}(f)$. Figure 6 shows this time-frequency construction. The diagnostic highlights that the spectral shape $S_{\mathrm{TEFT}}(f)$ is retained while the nonstationary storm envelope modulates the local spectral energy over time.

4. Conclusions

The first numerical results support the intended role of the framework as a bridge between coarse storm-wind information and structural reliability analysis. In the fixed-storm benchmark, TEFT-EPSD sampling restores unresolved short-duration wind peaks and produces a non-negligible displacement exceedance probability for the OpenSees tower model. In the stochastic storm example, the central top-node demand decreases because many sampled tracks are less severe than the fixed benchmark, but the upper response tail becomes substantially larger once storm-track, intensity, curvature, and background-wind variables are sampled together with the TEFT realization. At the illustrative 0.25 m displacement capacity, both 1000-sample experiments give the same exceedance estimate, while the stochastic storm ensemble retains nonzero exceedance probability at

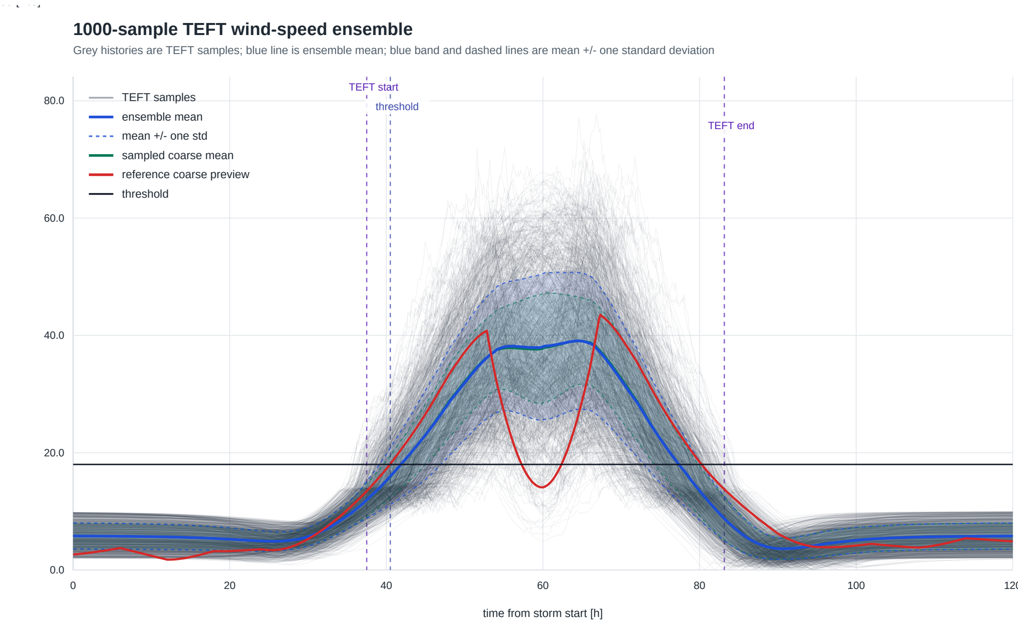

(a) Stochastic wind-speed ensemble.

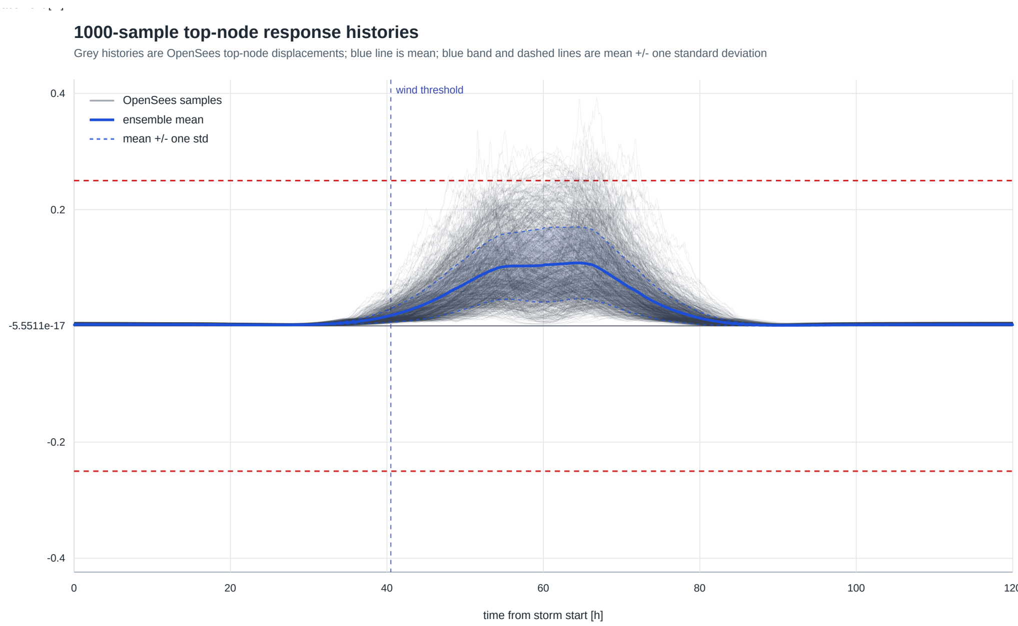

(b) Signed top-node displacement histories.

Figure 4. Wind input and structural response diagnostics for the 1000-sample stochastic tower run. The wind histories retain the threshold-triggered storm envelope, while the response histories show the signed OpenSees top-node displacement before extracting maximum absolute demand for the reliability calculation.

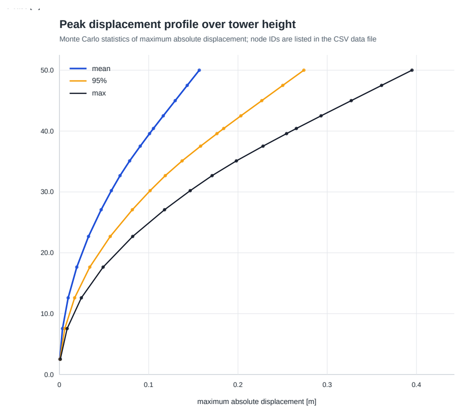

(a) Node-wise peak displacement profile.

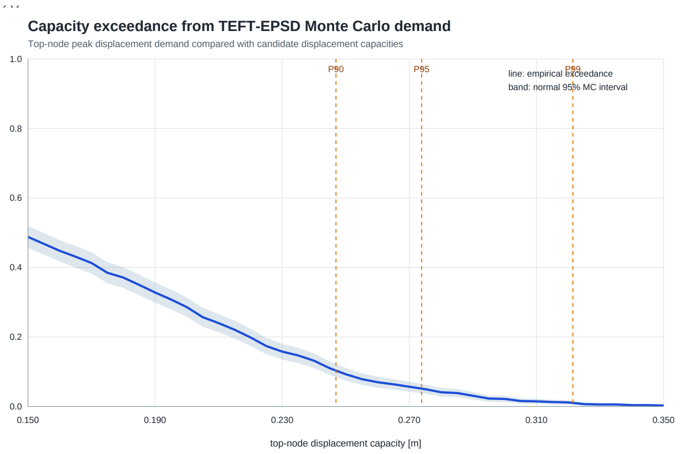

(b) Capacity exceedance curve.

Figure 5. Structural reliability diagnostics for the stochastic tower run. Panel (a) reports Monte Carlo statistics over height, while panel (b) reports the estimated exceedance probability as a function of displacement capacity. The vertical marker indicates the 0.25 m capacity used for the main reliability estimate.

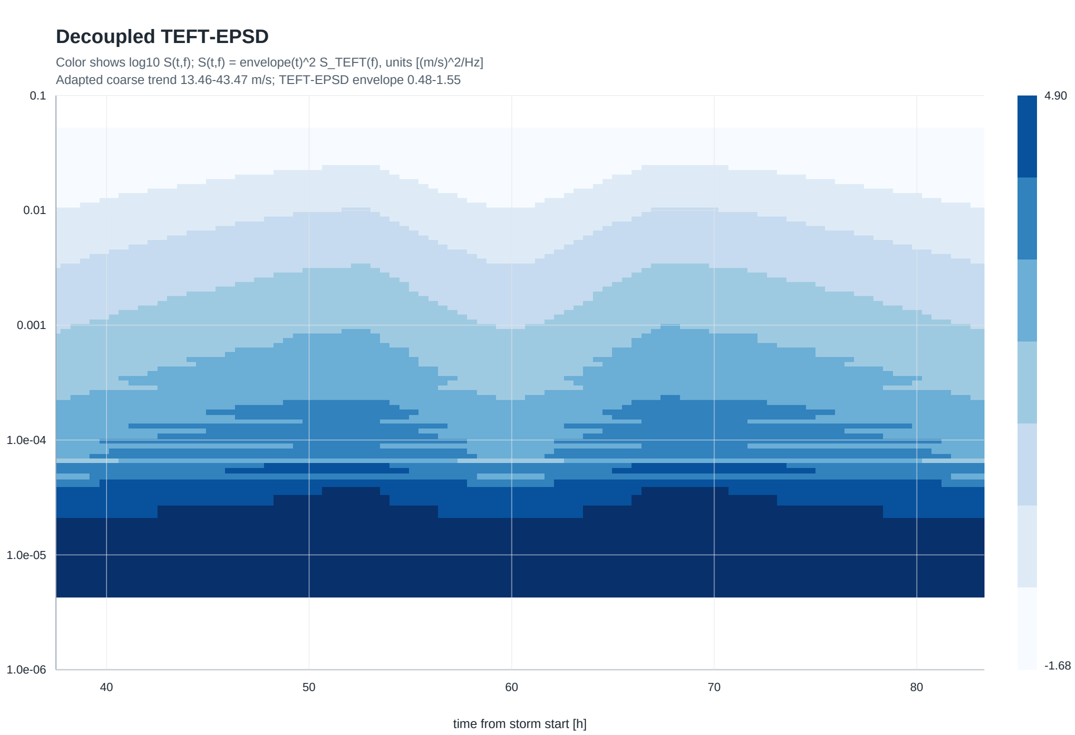

Figure 6. TEFT-EPSD heat map for the stochastic tower run. Color represents $\log_{10} S(t, f)$, illustrating how the stationary TEFT spectrum is modulated by the storm-scale envelope during the active window.

larger capacities. This redistribution of demand toward a rarer but more severe tail is the central reliability-relevant effect observed so far.

The present results should be interpreted as proof-of-concept demonstration cases rather than site-specific design values. The storm-variable ranges are bounded synthetic inputs, the displacement capacity is illustrative, and the final rare-event calculations are still being extended. Nevertheless, the computed response statistics show that the modular TEFT–storm–OpenSees workflow can produce traceable demand distributions, capacity-exceedance curves, and spectral diagnostics from coarse wind histories in a practical manner.

Acknowledgements

Marco Behrendt acknowledges financial support from the Alexander von Humboldt Foundation through a Feodor Lynen Research Fellowship. Marius Bittner acknowledges funding by dtec.bw - Digitalization and Technology, Research Center of the Bundeswehr. dtec.bw is funded by the European Union - NextGenerationEU.

References

Behrensdorf, J., Gray, A., Broggi, M., and Beer, M. (2023). UncertaintyQuantification.jl: A new framework for uncertainty quantification in julia. In *Proceedings of the 5th International Conference on Uncertainty Quantification in Computational Sciences and Engineering*, pages 419–436. doi: 10.7712/120223.10347.19810.

Behrensdorf, J., Gray, A., Perin, A., Grashorn, J., Luttmann, M., Fritsch, L., Belik, F., Schmidt, M., Broggi, M., Agarwal, G., Mett, F., Bittner, M., and Knipper, L. (2026). Juliauq/uncertaintyquantification.jl: v0.14.0. Software, Zenodo. `https://doi.org/10.5281/zenodo.18415973`.

Bezanson, J., Edelman, A., Karpinski, S., and Shah, V. B. (2017). Julia: A fresh approach to numerical computing. *SIAM Review*, 59(1):65–98. doi: 10.1137/141000671.

Bittner, M. (2026). Storm hazards simulation framework.

European Committee for Standardization (2005). EN 1991-1-4: Eurocode 1: Actions on structures – part 1-4: General actions – wind actions. Technical report, European Committee for Standardization, Brussels.

McKenna, F., Scott, M. H., and Fenves, G. L. (2010). Nonlinear finite-element analysis software architecture using object composition. *Journal of Computing in Civil Engineering*, 24(1):95–107. doi: 10.1061/(ASCE)CP.1943-5487.0000002.

Sun, Y., Bittner, M., Zhang, Y., and Beer, M. (2022). Simulation and risk evaluation of possible superstorms hitting europe's north sea coast. In Beer, M., Zio, E., Phoon, K.-K., and Ayyub, B. M., editors, *Proceedings of the 8th International Symposium on Reliability Engineering and Risk Management, ISRERM 2022*, pages 629–634, Singapore. Research Publishing Services. doi: 10.3850/978-981-18-5184-1_MS-19-105-cd.

Tambat, P., Bittner, M., Behrendt, M., and Beer, M. (2026). Data-driven modeling of synthetic wind speed signals with adaptive temporal resolution. SSRN preprint. Temporal Enhanced Fourier Transform (TEFT) manuscript; doi: 10.2139/ssrn.6531666; available at https://ssrn.com/abstract=6531666.

Tian, Z., Zhang, Y., Udo, K., and Lu, X. (2023). Regional economic losses of china's coastline due to typhoon-induced port disruptions. *Ocean and Coastal Management*, 237:106533. doi: 10.1016/j.ocecoaman.2023.106533.

Zhang, Y., Wei, K., Shen, Z., Bai, X., Lu, X., and Guedes Soares, C. (2020). Economic impact of typhoon-induced wind disasters on port operations: A case study of ports in china. *International Journal of Disaster Risk Reduction*, 50:101719. doi: 10.1016/j.ijdrr.2020.101719.